

GT2023-102031

The Impact of Multi-Scale Ceramic Matrix Composite Roughness on Heat Transfer and Boundary Layer Behavior

Peter H. Wilkins, Stephen P. Lynch, Karen A. Thole

Pennsylvania State University
Department of Mechanical Engineering
University Park, PA 16802, USA

ABSTRACT

Ceramic Matrix Composites (CMCs) can enable more efficient gas turbines relative to traditional nickel alloys resulting from enabling higher turbine entry temperatures that in turn benefit cycle performance. One negative effect of adding CMCs to the hot section is the introduction of a unique surface roughness due to the underlying weave topology. This surface roughness is generally at a macro scale compared with traditional turbine roughness such as deposits or erosion, which are well known to interact with the boundary layer development and increase convective heat transfer. In this study, scales representative of traditional turbine roughness in combination with macro scale weave roughness is investigated for convective heat transfer augmentation and boundary layer behavior. In addition to investigating the impact of the CMC roughness scales, 5 harness satin and twill weave patterns are studied to understand the differences between weaves. Heat transfer measurements are conducted in scaled up wind tunnel tests using a conjugate steady state analysis with freestream turbulence intensities of 0.5% and 24%. Boundary layer behavior is measured using Particle Image Velocimetry to capture cross-stream and streamwise planes. Compared to the 0° 5 harness satin surface, the twill surface has higher Stanton number augmentation, owing to the increased number and high density of flow facing features that disrupt the boundary layer. Additionally, the large-scale weave roughness and traditional small-scale turbine roughness act largely independent of one another.

NOMENCLATURE

5HS	five-harness satin (weave type)
A_f	projected frontal surface area
A_s	windward wetted surface area
A_t	total plan area
A_w	total upstream facing wetted surface area
C_p	specific heat at constant pressure
ES	effective slope, $(1/A_t) \int \partial h' / \partial y dA$
h	heat transfer coefficient, $h = q'' / (T_s - T_\infty)$

h'	variation in roughness elevation about the mean
k	thermal conductivity
k	roughness height
Ku	kurtosis, $((1/A_t) \int h'^4 dA) / (S_q^4)$
Pr	Prandtl number
q_{cond}''	heat flux from conduction
q_{rad}''	heat flux from radiation
R_a	arithmetic mean roughness (2D)
Re	Reynolds number, $Re = U_\infty * x / \nu$
S	reference surface area
S_a	arithmetic mean roughness (3D), $(1/A_t) \int h' dA$
S_f	total roughness frontal surface area
S_k	skewness, $((1/A_t) \int h'^3 dA) / (S_q^3)$
S_q	root mean square roughness, $\sqrt{(1/A_t) \int h'^2 dA}$
St	Stanton number, $St = h / (\rho C_p U_\infty)$
S_z	maximum roughness height, $\frac{1}{5} \sum_1^5 (h'_{max} - h'_{min})$
t	thickness
T	temperature
T_{Al}	aluminum temperature
T_s	plate surface temperature
Tu	streamwise turbulence intensity, $Tu = u' / U_\infty$
U	mean streamwise velocity
x	streamwise direction
y	wall normal direction
z	spanwise direction

Greek Symbols

δ	boundary layer thickness
λ	tow width
ν	kinematic viscosity
ρ	density

Subscripts

air	property of air
CMC	property of CMC surface test plate
i	interface
0	property of a flat surface
∞	freestream

Superscripts

- ‘ fluctuating/rms value
- laterally averaged
- = area averaged

INTRODUCTION

Ceramic matrix composites (CMCs) have the potential to improve gas turbine efficiency while also reducing component weight. Improvements in efficiency are realized through a combination of higher turbine entry temperatures and reduced cooling, both of which are enabled by the higher temperature capabilities of CMCs relative to nickel alloys. Reduced weight is another advantage of CMCs where their reduced density can result in components that are one-third the weight relative to nickel components [1,2].

New nickel alloy components can be machined to finishes that are very smooth with surface roughness on the order of $Ra=1.5\text{ }\mu\text{m}$ [3]. However, CMC components have additional machining challenges that stem from their high hardness, brittle behavior, anisotropic mechanical and thermal properties, and heterogeneous structure [4]. This structure is byproduct of manufacture of CMCs, which are typically created using an infiltration process such as polymer infiltration pyrolysis or chemical vapor infiltration. Generally, infiltration techniques start with fibers being laid up and molded to the desired geometry, then coated with an interphase layer. Next, fibers are infiltrated with a preceramic fluid that is then baked, converting it into a ceramic [5]. Difficulties in machining this final structure can lead to surfaces with roughness from the weave pattern that may even impact the flow when coated with an environmental barrier coating (EBC), due to the large length scales. In addition to weave roughness, CMC components will also be subjected to the same conditions as traditional components, leading to in-service erosion and deposition buildup. It is unclear how these scales of roughness might interact.

In this study, convective heat transfer augmentation and flowfields over two CMC weave patterns, a 2x2 twill and a 5 harness satin (5HS), are evaluated at two freestream turbulence conditions. The 5HS surface is evaluated with its long exposed tows positioned 45° relative to the oncoming flow, filling the gap between the 0° and 90° orientations tested by Wilkins et al. [6]. The twill pattern is tested at both 0° and 45° orientations at both 0.5% and 24% freestream turbulence intensities. Additionally, a k-type roughness is superimposed onto the 0° twill weave to simulate deposition and erosion to the CMC surface. This is then compared to the k-type roughness baseline to understand how in service use may alter roughness characteristics for CMC parts.

BACKGROUND

The effect of surface roughness varies substantially depending on the surface type, with each roughness type exhibiting unique behavior that so far has eluded a universal scaling. The boundaries that define the differences between types of roughness are not firm, however k-type roughness can be defined as stochastic roughness with $k < \delta$ and the effective

roughness is proportional to the roughness height, k [7]. This is the most widely studied type of roughness where an increase in roughness height leads to greater drag and heat transfer [8–11]

Owing to the prevalence and negative impact of surface roughness in gas turbines, several studies have investigated a variety of roughness types present within engines. One study by Bogard, et al. [3] investigated how turbine roughness impacts heat transfer augmentation. Roughness was characterized by measuring 12 locations across two aero engines using arithmetic mean roughness Ra , and the shape factor:

$$\Lambda_s = (S/S_f)(A_s/A_f)^{1.6} \quad (1)$$

defined by Sigal and Danberg [12]. From this experiment Bogard, et al. found roughness with shape factors between 18 and 74 increased average heat transfer between 50-60% relative to a smooth surface at 0.3% freestream turbulence. At high freestream turbulence levels of 10% and 17% Bogard, et al. found that heat transfer augmentation from elevated turbulence and roughness were additive, resulting in up to a 100% increase in heat transfer relative to a smooth surface with low freestream turbulence.

Expanding the variety of turbine roughnesses surveyed, Bons et al. [13] performed an extensive review, including roughness from deposits, erosion, pitting, and spallation. These surfaces had a wide range of roughness characteristics, with shape factors ranging from 21 to 1130, Ra ranging from $4.1\mu\text{m}$ to $33.2\mu\text{m}$ and similarly wide ranges for maximum peak to valley height, skewness, and kurtosis. From this surface characterization study a follow up study by Bons [14] investigated the impact of six rough surfaces on heat transfer and skin friction augmentation. Heat transfer augmentation was found to be between 10-50% higher and skin friction was found to be between 30-300% higher for the roughness relative to a smooth surface. Additionally, Bons found that levels of high freestream turbulence had a synergistic impact leading to 5% more heat transfer than would be expected by adding the roughness and turbulence separately.

The wide ranges in both heat transfer and skin friction for the roughness tested by Bogard, et al. [3], Bons [14], and several others [15–18] led to a thorough review by Bons [19]. Generally, roughness of any kind increases heat transfer and skin friction relative to a smooth surface in low freestream turbulence. However, one of the key points Bons highlighted is the need for individual roughness correlations for individual roughness types, complicating the relationship between statistical roughness measurements and “equivalent sandgrain roughness” or similar fluid-relevant characterizations. This uniqueness makes it difficult to predict the impact of uncharacterized roughness.

Understanding how roughness scales impact flow fields is one piece in improving the ability to predict the impact of uncharacterized roughness. Mejia-Alvarez and Christensen [20] investigated the scales needed to reproduce a surface characterized by Bons, et al. [13] and then measured by Bons [14]. Mejia-Alvarez and Christensen partially reconstructed roughness profiles by representing the roughness using

simplified models that captured the 5 largest and 16 largest scales. It was found that the 16 mode model largely matched the flowfield and wall shear stress of the true surface representation with fractional surface content of 95%, indicating most of the surface features had been recreated. This study, in addition to an earlier related study by Johnson and Christensen [21], reinforce the concept that there is a limit of roughness scale size below which it will have a negligible impact.

However, once again this is not a universal conclusion for surface roughness; some very large roughness scales can also have a negligible impact on heat transfer and skin friction. These large scales are associated with a mean absolute streamwise gradient of a rough surface, known as effective slope, of less than 0.35 which leads the surface topography regime to change from k-type roughness to waviness [22]. The presence of waviness on a surface can lead to lower friction and heat transfer impacts than traditional roughness metrics like Ra would suggest [23]. Barros, et al. [24] investigated this phenomenon after performing measurements on several rough surfaces that varied significantly from correlations. By applying a range of high pass filters to three systematically generated surfaces, Barros, et al. removed the lower frequency roughness, creating surfaces that more closely matched the correlation by Schultz and Flack [22]. Nugroho et al. [25] investigated scaling effects of roughness from a painted ship hull to better understand the relationship between waviness and boundary layer size. From this investigation Nugroho, et al. reinforced the conclusions from Barros, et al. [24] that found as in-plane roughness wavelength approaches the boundary layer thickness, surfaces no longer behave like k-type roughness.

CMC specific roughness has been studied only recently to better understand how the large scales of CMC weaves impact heat transfer and flowfield performance. Two studies by Krishna and Ricklick investigated the heat transfer impact of jet impingement on CMCs and found that resolution issues from manufacturing of their surfaces was a dominant factor in their experiments [26,27].

Wilkins, et al. [6] performed a study investigating the impact of CMC surfaces on heat transfer and flowfield behavior. In this study Wilkins et al. scaled up a 5HS weave geometry and investigated it at two orientations. It was found that when long exposed tows were aligned parallel to the freestream, area averaged heat transfer was similar to a smooth surface. However, localized regions of elevated heat transfer were present where flow impinged on protruding tows at tow transitions. Offsetting these regions of elevated heat transfer, flow separating off the back of tows at tow transitions led to a reduction in heat transfer. Alternatively, when the long-exposed tows were oriented perpendicular to the freestream they acted similarly to trips and led to higher heat transfer than the streamwise oriented surface. A numerical study by Wilkins et al. [28] confirmed that the perpendicularly oriented tows had higher heat transfer augmentation than the parallel oriented tows, but the RANS model over and under predicted heat transfer augmentation for the 0° and 90° weaves respectively.

Many studies have investigated the impact that roughness

has on heat transfer and flow field behavior. This study aims to specifically understand impacts of potential CMC weave patterns including weave geometries at 45° to the oncoming flow. Additionally, over the life of a gas turbine, roughness from erosion and deposition develops on components and understanding how these two roughness scales interact will contribute to understanding the in-service life of CMC components. This is investigated through the superposition of a k-type roughness onto a CMC geometry and comparing the resulting performance to the individual macro (CMC) and micro (k-type roughness) surface elements. Lastly, turbine components that may benefit the most from CMC materials are exposed to high levels of freestream turbulence, which is investigated for a few select cases.

DESCRIPTION OF SURFACE GEOMETRY

Two CMC weave patterns are investigated in this study. Both are mathematically defined and are generated using the open source software TexGen [29] to create repeating unit cells (RUCs). The first is a 5 harness satin (5HS) geometry shown in Figure 1a that is modified from Nemeth, et al. [30] and defined in Wilkins et al. [6]. The second is the 2x2 twill weave pattern in Figure 1b, which is defined to match tow parameters with the 5HS. Both have a tow width (at turbine engine scale) of $\lambda=1.125$ mm and fabric thickness of 0.375 mm. The bottom halves of both weave patterns are filled to eliminate any overhanging surfaces that are not visible from directly above the weave. The RUCs are then scaled up 30X to match the scale of the surface in the lab experiment to the expected Reynolds number in a gas turbine.

A k-type surface roughness was generated using a linear compilation of five sinusoids to generate a rough surface with multiple scales. The roughness characteristics, shown in Table 1, were chosen to replicate the roughness statistics from Bons [13] and Bogard [3]. The final surface is a superposition of the k-type roughness onto the 0° twill weave pattern. To create this surface, both surfaces are first adjusted so their mean roughness height is

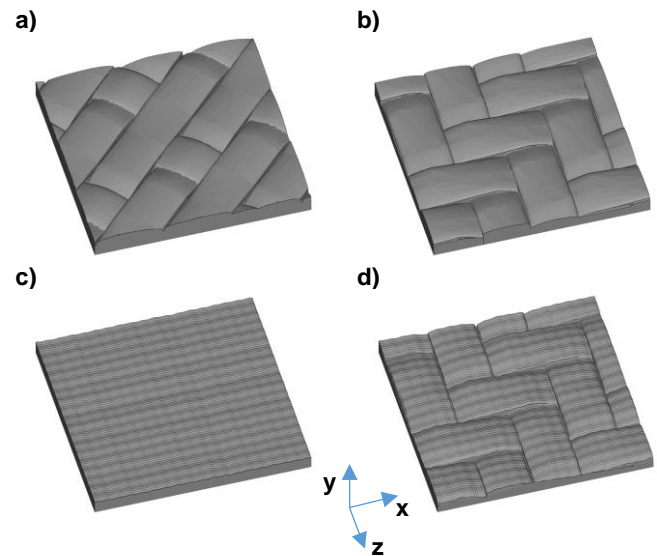


Figure 1: Perspective views of the a) 45° 5HS, b) 0° Twill, c) flat surface k-type roughness, and d) 0° Twill + k-type roughness

Table 1. Turbine Scale Surface Roughness

Surface	0° 5HS	0° Twill	k-type	0° Twill + k-type
Sa (μm)	38	55	9.9	37
Sq (μm)	46	63	12.4	45.5
Sz (μm)	201	187	105.1	276
Sk	-0.60	-0.51	0	-1.03
Ku	2.46	1.95	3.0	3.69
Λ _s	N/A	N/A	59.8	52.8
ES [9]	N/A	N/A	0.28	0.28

aligned to $Y=0$ in the XZ plane. Then control points are generated by interpolating the Y heights for each surface onto a grid with $250\ \mu\text{m} \times 250\ \mu\text{m}$ spacing in the $X-Z$ plane. Finally, the Y -component of the k -type rough surface's control points is added to the Y -component of the 0° twill control points, resulting in a new surface with both roughness types.

EXPERIMENTAL FACILITY AND METHODS

Heat transfer and flowfield experiments are conducted in the recirculating wind tunnel facility described in detail by Eberly, et al. [31] and Wilkins, et al. [6]. Test section dimensions are $0.3\text{m} \times 0.3\text{m} \times 1.2\text{m}$ with a maximum freestream velocity of 17 m/s and the ability to adjust freestream turbulence intensity from 0.5% to 24.3% at $x/\lambda=4.5$. This is achieved in the same approach as Schroeder and Thole [32], through the use of vertical bars with a diameter of 1.125λ located $x/\lambda=-7.7$ upstream of the leading edge. All of the experiments are conducted with a freestream temperature of $20\ ^\circ\text{C}$ maintained using a chilled water heat exchanger.

The test section is the same as used by Wilkins et al. [6] and is shown in Figure 2. At the leading edge of the test surface an elliptical leading edge is present, below which is a boundary layer suction system, generating a new boundary layer. Located at the transition point between the elliptical boundary layer and the surface, defined as $x/\lambda=0$, is a boundary layer trip to ensure a turbulent boundary layer.

Test surfaces are printed on a Photocentric Pro 3D printer, with pixel resolution of $137\ \mu\text{m} \times 137\ \mu\text{m}$ and a layer height of

$50\ \mu\text{m}$ in Photocentric Hard Black resin. Thermal conductivity of the resin is measured by the authors to be 0.208 W/m-K and an average test plate thickness of 9.5 mm minimizing uncertainty by creating a temperature difference of $10\ ^\circ\text{C}$ between the freestream and plate surface and $30\ ^\circ\text{C}$ between the plate surface and the heat spreader. The top of the rough surfaces is painted with a thin coat of matte black spray paint with an emissivity of 0.95 [33]. This 3D printed surface is the top layer of a five-layer stack that makes up the bottom wall of the test section.

A thin layer of silicone rubber is placed below the 3D printed surface that has a thermal conductivity of 0.2 W/m-K and a thickness of 1.58 mm . This silicone layer acts as a thermal bridge, ensuring complete thermal connectivity between the 3D printed surface and the next layer, an aluminum heat spreader. The heat spreader is a 2 cm thick aluminum plate with thermocouples inlaid into both the top and bottom, where heaters are also attached. The aluminum plate spreads out the electric heat supplied to its bottom, leading to a constant temperature condition across the top that is within $\pm 0.5\ ^\circ\text{C}$. The heaters along the bottom are split into three zones. This multi-zone approach allows for the heater near the leading edge to output a high heat flux while allowing the heaters downstream to maintain a lower heat flux resulting in the uniform temperature condition at the top of the heat spreader. The final layer of the stack is 7.6 cm of low conductivity foam in addition to a layer of 0.6 cm foam around the edges of the stack to minimize conduction losses.

Heat Transfer Measurements

Heat transfer measurements are taken using the method described in Wilkins et al. [6], and is similar to the method used by Gritsch et al. [34] to determine heat transfer coefficients near film cooling holes. A FLIR SC620 infrared camera is used to measure the surface temperature of the surfaces at four locations in the streamwise direction. Images are calibrated in-situ using multiple visible thermocouples in each image, then are stitched together to create a temperature map across the entire surface. Temperature is also measured on the top of the aluminum heat spreader using ten inlaid thermocouples. With known temperatures on the top and bottom of the rough surface + silicone assembly, and with the material properties of the assembly components known, heat flux at the surface can be calculated. The one-dimensional equivalent of this calculation is:

$$q''_{\text{cond}}(x, z) = \frac{T_{\text{Al}} - T_s(x, z)}{\frac{t_{\text{CMC}}}{k_{\text{CMC}}} + \frac{t_i}{k_i}} \quad (2)$$

To account for the three-dimensional nature of the surface roughness, however, a computational model is used. The finite element model is analyzed in STAR-CCM+ 2021.3 using the STL model that is used to print the surface, which had a resolution designed for the 3D printer. Mesh size for the model is determined from the grid resolution study conducted by Wilkins et al. [6]. From the model, the top surface heat flux due to conduction through the 3D printed material is used to calculate

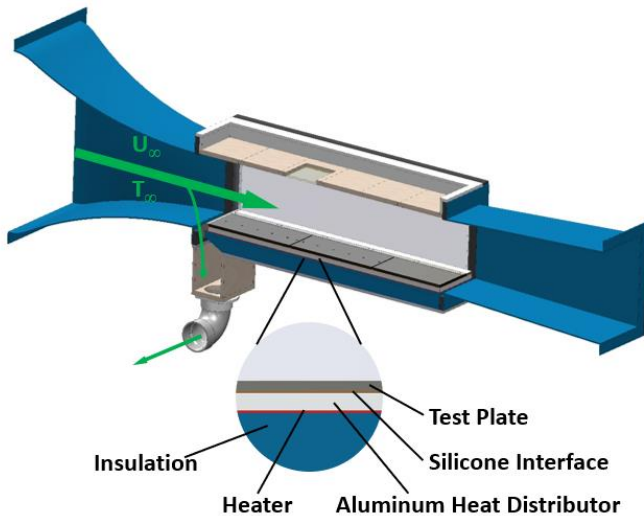


Figure 2. Cross section of the test section and expanded view of the five layers that compose the composite endwall

local heat transfer coefficients across the surface using equation 3:

$$h(x, z) = \frac{q''_{\text{cond}}(x, z) - q''_{\text{rad}}(x, z)}{T_s(x, z) - T_\infty} \quad (3)$$

Note that the surface heat flux lost due to radiation in the experiment, at approximately 8%, is accounted for. Local Stanton number is then calculated from the local heat transfer coefficient.

Flowfield Measurements

Flowfield measurements are taken along two different planes using particle image velocimetry (PIV). The wind tunnel is seeded using Di-ethyl-hexyl-Sebecat (DEHS) as the tracer particles using an aerosol generator creating particles with a mean diameter of 1 μm and a maximum Stokes number of 0.01 [32,35]. Tracer particles are illuminated using a dual-head Nd:YLF laser with 20 mJ per pulse and a pulse width of 170 ns that generates a laser sheet with a thickness of 1mm.

Stereo PIV measurements to obtain all three velocity components in a plane are taken at a cross-plane located at $x/\lambda=9$. Two cameras with a resolution of 1280 x 1024 pixels are angled at 45° to the measured plane as shown in Figure 3. The focus plane mis-match is corrected through the use of a Scheimpflug adapter on each camera, providing a resolution of 0.12 pixels/mm. Stereo images are taken at a sampling rate of 500 Hz per image pair over 4000 samples to achieve statistical convergence. The time between images in an image pair is 15 μs , to allow for the particles to travel 1/4th of the laser sheet thickness. Stereo measurements are analyzed in DaVis 10.2 where a planar self-calibration is applied to refine the spatial calibration. A multi-pass vector scheme is used with an initial 96x96 pixel interrogation window and a final interrogation window size of 32x32 pixels with a 75% overlap. Vector post processing is used to remove and iteratively replace vectors with correlation values less than 0.4, resulting in 15% of the vectors

being replaced. In less than 1% of cases the correlation value criteria are not met through vector replacement and interpolation is used in the interrogation window.

Streamwise two-dimensional PIV measurements are taken in the XY plane at $z/\lambda=1.5$ or $z/\lambda=1.3$ depending on the surface features the laser sheet passes over. This set up has two side-by-side cameras that are oriented perpendicular to the laser sheet to extend the field of view in the x direction as shown in Figure 4 with a resolution of 0.12 pixels/mm. The sampling rate is increased to 2.4 kHz per image pair for better tracking of flow structures as the flow progress downstream. Time between image pairs is 30 μs to allow particles to travel 5 pixels per image pair. DaVis 10.2 is also used for the two-dimensional measurements, with the multi-pass vector scheme progressing from a 96x96 pixel spatial resolution window to a 32x32 pixel window with a 75% overlap. Like the stereo measurements, vector post processing is used to iteratively remove and replace vectors with correlation values less than 0.4. In interrogation windows where no correlation value 0.4 or greater is found, interpolation is used fill in the window.

Uncertainty Analysis

Heat transfer bias and precision uncertainties are calculated using the methods described in Moffat [36] and Figliola and Beasley [37] respectively, where all precision uncertainties are calculated using a 95% confidence level. Stanton number calculations have a bias uncertainty of $\pm 14.1\%$ and a precision uncertainty of $\pm 3.7\%$, resulting in a total uncertainty of $\pm 14.6\%$. Based on a detailed uncertainty analysis, the measurement of the top surface temperature is the largest contribution, followed by the conductivity of the plate material. Flow field measurement uncertainty is calculated in DaVis using the method described by Wieneke [38], producing an average velocity component uncertainty of $\pm 5\%$ across the entire domain, including both the freestream and boundary layer regions.

RESULTS AND DISCUSSION

Heat transfer and PIV measurements are taken across five rough surfaces at two different freestream turbulence levels.

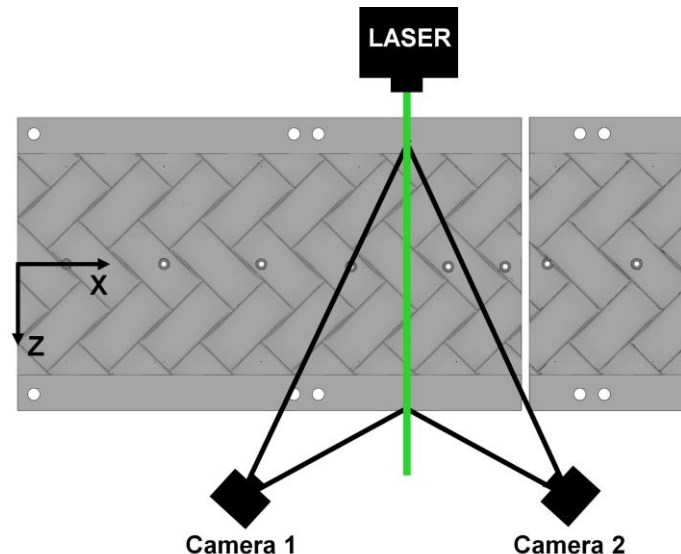


Figure 3. Stereo PIV setup

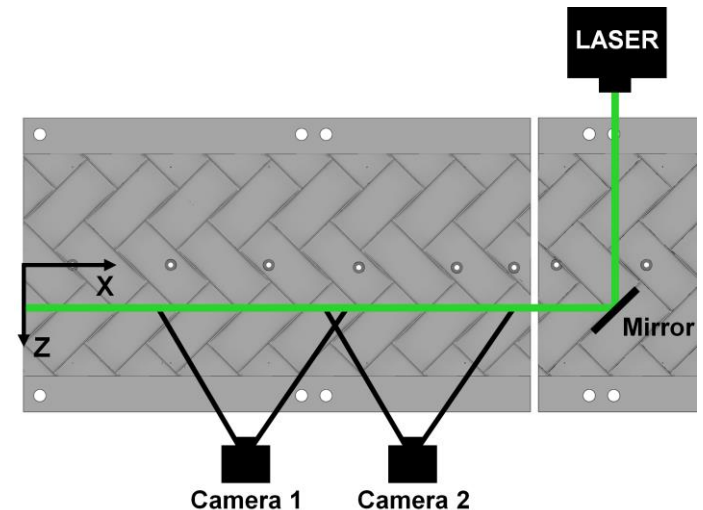


Figure 4. 2D Planar PIV setup

Heat transfer is measured across the entire length of the test section, with a small area cropped near the middle where the seam between the two test plates is located. Above the surface flowfield measurements across the first plate help identify the mechanisms responsible for the local heat transfer variations.

Low Freestream Turbulence Heat Transfer

Heat transfer augmentation contours in Figure 5 show the local increases and decreases in heat transfer relative to a smooth surface across the tested surfaces. Figures 5a and 5b from Wilkins, et al. [6] are established weave patterns from which to compare the tested roughness against. The 0° 5HS surface in Figure 5a has several important behaviors that contribute to regions of elevated and reduced heat transfer over weave surfaces. In regions where elevated heat transfer is present, flow impinges onto the front of tows located directly downstream of tow transitions. Regions of reduced heat transfer on the trailing edges of tows are caused primarily by flow separation. Similar physical mechanisms are present over the 90° 5HS in Figure 5b where the increase in forward facing tow surface area results in comparatively more heat transfer than the 0° surface.

Expanding upon the study by Wilkins, et al. [6], Figure 5c shows the 5HS surface at a 45° angle relative to the oncoming flow. Like the 90° 5HS surface, there is heat transfer augmentation across the leading edges of all of the tows; however, the magnitude of the augmentation is less than for the 90° 5HS. Heat transfer augmentation also increases as the flow becomes more developed. The surface feature that generates the greatest heat transfer is at the transition of a large tow to small tow. Directly downstream on the back half of the small tows there is a slight downward slope where there is negative heat transfer augmentation, similar to negative heat transfer regions in Figure 5a.

Similar to 5HS surfaces in Figures 5a-c, the 0° twill in Figure 5d has elevated heat transfer on upstream facing surfaces relative to a smooth surface. Downstream facing surfaces on the 0° twill have reduced heat transfer in a similar manner to the 5HS surfaces. Over the 0° twill the regions of positive heat transfer are more prevalent than over the 0° 5HS as a consequence of the greater number for forward facing surfaces that the oncoming flow can impinge on.

Rotating the twill 45° creates the most distinctive heat transfer distribution across the test matrix, shown in Figure 5e. The surfaces in Figures 5a-d generally have increased heat transfer across tow leading edges and reduced heat transfer on trailing edges where there is a slight downward slope. Instead, the 45° twill is split into two zone types along the streamwise direction, with increased heat transfer on upstream pointing V-shapes, referred to here as chevrons, and reduced heat transfer along the downstream facing chevrons. Along the leading edge of the upstream facing chevrons the greatest heat transfer is located where two tows intersect to create a point. Moving away from this point, heat transfer augmentation diminishes in both the lateral and streamwise directions along the tow, to the downstream facing chevrons where the minimum heat transfer across the surface is located.

Figure 5f shows the local heat transfer augmentation for the k-type roughness surface. The smaller scale of the k-type roughness creates a surface that has many local variations rather than the macro-scale trends present over the weave surfaces.

Combining the k-type roughness and 0° twill creates the surface shown in Figure 5g that has both high heat transfer at the tow leading edges and significant local variation. The k-type roughness in Figure 5g exhibits the same banded high and low heat transfer regions as Figure 5f, but compared to Figure 5f the peak augmentation values are more extreme for both high and low heat transfer.

Lateral averages of the 0° twill, k-type roughness, and 0° twill + k-type roughness surfaces in Figure 6 show heat transfer changing with increasing Reynolds number (distance along the plate) relative to the correlation for a smooth surface with constant heat flux. Over the 0° twill, the location of tows can be clearly identified, with heat transfer spiking at tow leading edges and then dropping along the tow surface as it progresses downstream. This cycle then repeats over the next tow. K-type roughness has more local variations with a smaller range of heat transfer values than the 0° twill surface. More consistent heat transfer over the k-type roughness also keeps the lateral average above the smooth baseline. The 0° twill + k-type roughness surface has heat transfer characteristics of each of its constituent surfaces. Large scale behavior across the tows is similar between the 0° twill and 0° twill + k-type surfaces, where both have similar periodicity and similar maximum heat transfer values at the leading edge. Area averaged heat transfer augmentation for the tested rough surfaces and select roughness from Bons [14] are shown in Figure 7. The 0° and 45° 5HS have near zero heat transfer augmentation on an area average basis, despite the local variations in Figures 5a and c. The 0° twill has 7% more heat transfer than a smooth surface and 0° 5HS surface but is still lower than the 90° 5HS [6]. Rotating the twill 45° more than doubles heat transfer augmentation relative to the 0° twill. The unintentional creation of the chevron shape in the 45° twill creates the greatest heat transfer augmentation of all of the weave patterns tested.

The k-type roughness in Figure 7 has a heat transfer augmentation of 10%, higher than most of the weaves tested but lower than the rough surfaces investigated by Bons [14]. The k-type roughness surface likely underperforms relative to expectation and Bons [14] due to the use of a basis shape (sinusoid) with a kurtosis of zero, and the incorporation of relatively large scales in the calculation of roughness statistics. In Figure 5f only the two smallest scales (0.2327λ and 0.0465λ) in the k-type roughness visibly change local heat transfer while the three larger scales do not have a clearly visible impact. Isolating the two smallest scales, a maximum roughness height of $47\text{ }\mu\text{m}$ (at engine scale, $1\times$) is calculated and is substantially less than the surface roughness targeted in Table 1. Using the correlation from Flack and Shultz [40], a predicted $k_s = 19\text{ }\mu\text{m}$ at engine scale is well within the transitional roughness regime and indicative of the lower than expected heat transfer over the surface. Importantly, the goal of this study is to understand the impact of adding small scale roughness to CMC weave patterns

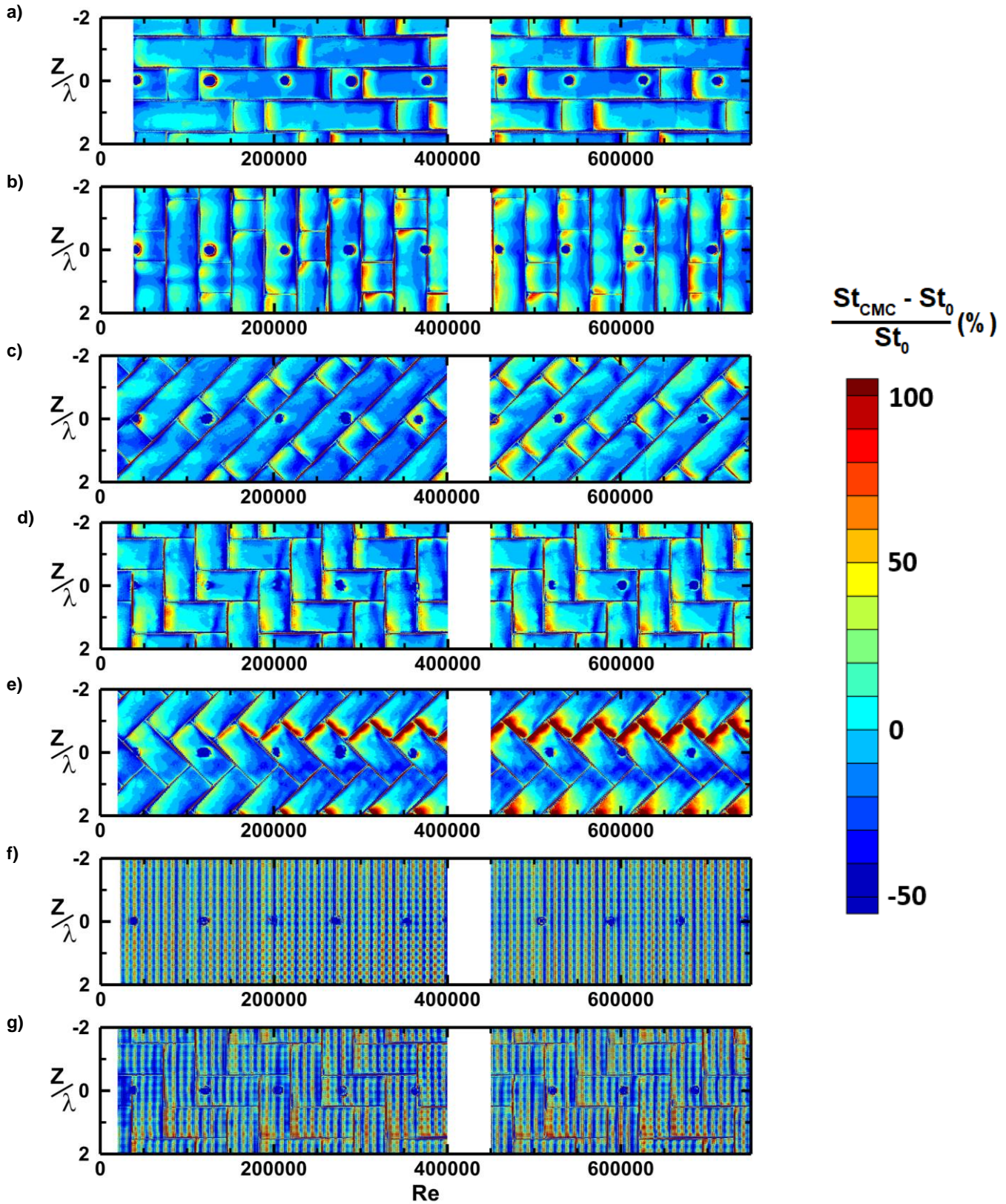


Figure 5. Local heat transfer augmentation contours for the a) 0° 5HS surface [6], b) 90° 5HS surface [6], c) 45° 5HS surface, d) 0° twill surface, e) 45° twill surface, f) k-type roughness surface, g) 0° twill surface + k-type roughness surface

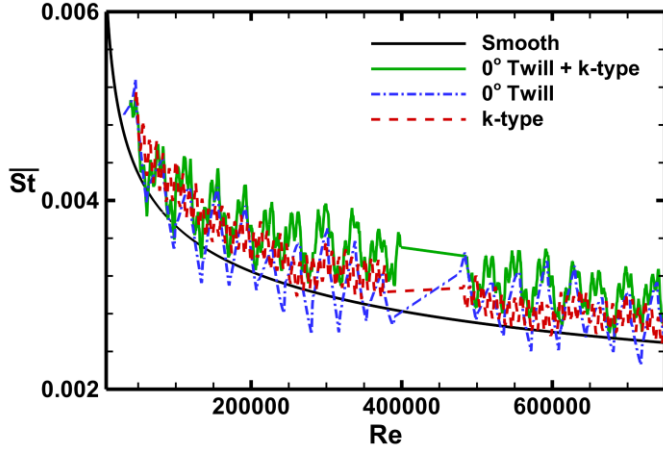


Figure 6. Laterally averaged Stanton number across select CMC surfaces across a range of Reynolds numbers, smooth curve is a correlation for turbulent flow over an isothermal smooth surface, $St = 0.0296 \cdot Re^{(4/5)} \cdot Pr^{(1/3)} / (Re \cdot Pr)$ [39]

and the k-type roughness modeled here, while not producing augmentation levels similar to Bons [14], does not prohibit investigating this behavior.

The composite 0° twill + k-type roughness surface has higher heat transfer augmentation than each of its individual constituents, at 16%. Adding the individual heat transfer augmentation values of the 0° twill and k-type roughness together results in heat transfer augmentation of 16%, identical to the combined surface. In Figures 5g and 6 the 0° twill + k-type roughness surface exhibits characteristics of both constituent surfaces. This independence likely arises from the large difference in length scales of the dominating scales of each roughness type, where the 1x length scale of the weave is 1.125mm and the dominant 1x length scales of the k-type surface are between 0.26 mm and 0.05mm. The lack of overlap allows

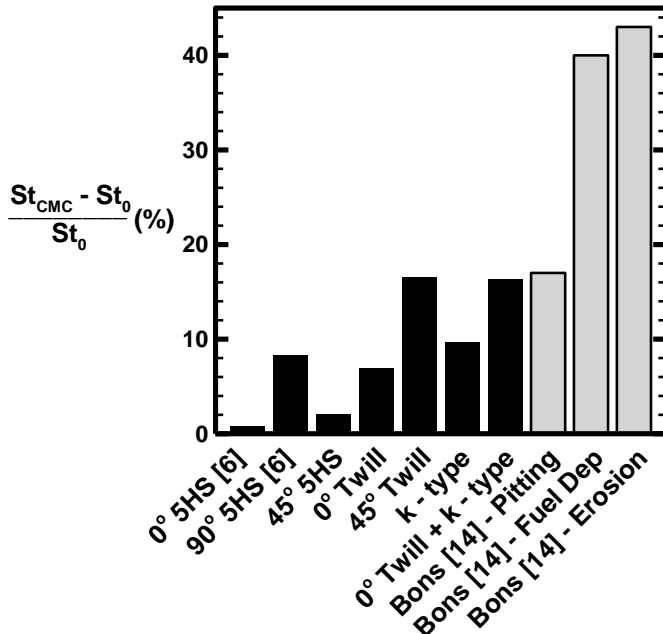


Figure 7. Area averaged Stanton number augmentation

the traits of each surface to be exerted independently, enabling additive superposition to accurately predict the heat transfer of the combined surface.

High Freestream Turbulence Heat Transfer

Laterally averaged heat transfer values over the combined 0° twill + k-type roughness surface at $Tu=0.5\%$ and $Tu=24\%$ are shown in Figure 8. It should be noted that the slight misalignment in the sawtooth heat transfer pattern between low and high turbulence cases is due to a slightly lower freestream velocity (and thus change in local Reynolds number for a fixed surface geometry) present in the high turbulence cases resulting from wind tunnel limitations. Increased heat transfer in elevated freestream turbulence is present across the high freestream turbulence case shown. However, the increase in heat transfer generated by elevated turbulence is greatest near the leading edge, where the freestream turbulence is the highest, and then degrades across the surface. The changing impact of elevated freestream turbulence is a consequence of the decaying turbulence intensity as the flow progresses downstream.

Across the three surfaces investigated at elevated freestream turbulence, all three have comparable increases in area averaged heat transfer augmentation relative to a smooth surface as shown in Figure 9. The smallest increase in heat transfer is over the k-type roughness while the largest is over the 0° twill + k-type roughness surface. However, the increase in heat transfer due to elevated freestream turbulence is nearly identical across all three surfaces.

Low Freestream Turbulence Flowfields

Wilkins, et al. [6] measured the boundary layer behavior over the 0° and 90° 5HS surfaces and identified the primary mechanisms that cause positive and negative heat transfer over CMC weave surfaces. Figure 10 shows where representative surface features with flow impinging along the red regions creating positive heat transfer augmentation, and separating in the blue regions creating regions of negative heat transfer

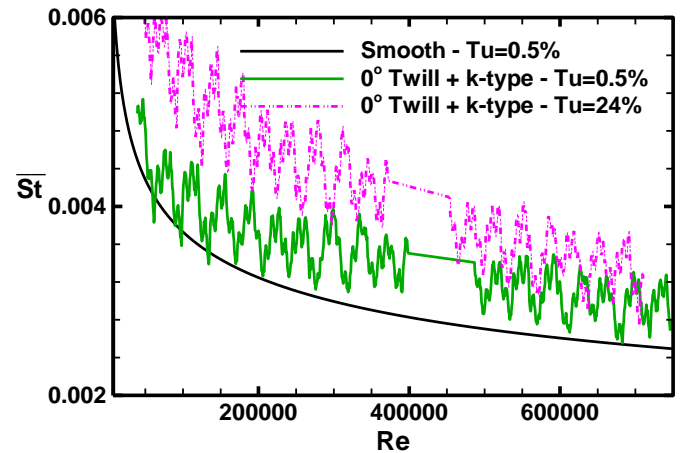


Figure 8. Laterally averaged Stanton number across select CMC surfaces for different freestream turbulence levels, smooth curve is a correlation for turbulent flow over an isothermal smooth surface, $St = 0.0296 \cdot Re^{(4/5)} \cdot Pr^{(1/3)} / (Re \cdot Pr)$ [39]

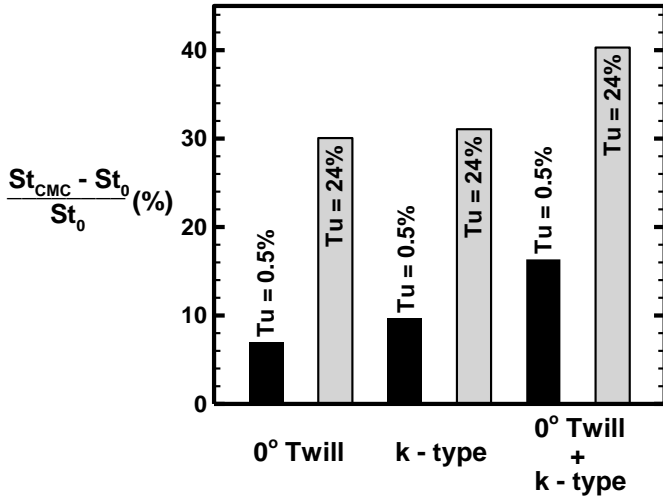


Figure 9. Area averaged Stanton number augmentation

augmentation. These physical mechanisms are also present over the CMC surfaces tested in this study.

PIV measurements are taken across all five rough surfaces tested in this study, in addition to a smooth baseline surface to compare against. The cross-plane in Figure 11a over the smooth surface shows the streamwise velocity with a uniform boundary layer across the span, and near wall velocities approaching zero.

Over the 45° 5HS surface in Figure 11b there is an increase in boundary layer thickness near $Z/\lambda=0.75$ directly downstream of a large flow facing feature at a tow transition. This is a result of the flow impinging onto the larger tow and being forced up into the boundary layer. Across the span of the 0° twill in Figure 11c the flowfield is mostly uniform, but with a thicker boundary layer than the smooth or 45° 5HS surfaces. This is a result of the regular flow disturbance of the large spanwise oriented tows that occur frequently in this geometry. The low near wall velocity is a consequence of the separation off the preceding tow as indicated in Figure 10.

The streamwise velocity plane over the 45° twill surface in Figure 11d is located directly before the apex of a downstream facing chevron where reduced heat transfer was observed, centered around $Z/\lambda=1$. To either side of the downstream facing chevron there are bulges in the boundary layer, associated with a counter rotating cell that is created by the adjacent upstream

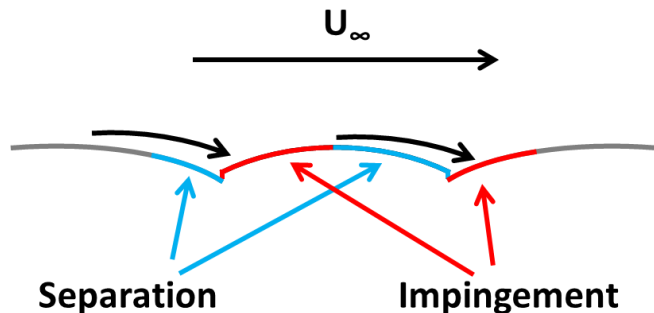


Figure 10. Diagram of flow impingement and separation over CMC wave surfaces

facing chevrons in a manner similar to the flowfield established by V-shaped rib turbulators [41]. The cells pull freestream air down onto the upstream facing chevrons increasing local heat transfer, and transport heated near-wall air to the downstream facing chevrons reducing local heat transfer.

Figure 11e shows the mostly uniform velocity profile over the k-type roughness. Compared to the smooth surface boundary layer thickness of 0.5λ in Figure 11a, the k-type roughness in Figure 11e has a slightly thicker boundary layer at 0.53λ . This behavior aligns with expected roughness behavior, where the roughness impacts the near wall region shifting the log region further from the wall but maintaining outer layer similarity.

As might be expected, the streamwise velocity over the 0° twill + k-type roughness surface in Figure 11f has a thicker boundary layer than either the 0° twill or the k-type roughness. Additionally, the near wall region in the 0° twill + k-type surface has somewhat irregular low-velocity bumps that appear to correspond to the larger wavelength roughness features in the k-type reconstruction. The local flowfield over those high wavelength features of the k-type roughness may be influenced by the regular separation and reattachment phenomenon of the 0° twill tows, since the plain k-type surface does not show similar evidence of local low-velocity regions.

Streamwise oriented measurements along the X-Y plane in Figure 12 highlight the differences in developing boundary layer thickness and the local impacts of tow-to-tow transitions. The baseline smooth surface in Figure 12a slowly develops a boundary layer as it progresses downstream. In contrast, Figure 12b shows that the 45° 5HS surface already has a thick boundary layer across the surface at the start of the measurement region, which develops irregularly as the flow accelerates and decelerates over the tows.

The 0° twill surface in Figure 12c is generally similar to the smooth surface aside from a few localized differences. Globally the boundary layer over the 0° twill has slightly lower near wall velocities compared to the smooth surface but is similar in thickness. Along the tow-to-tow transitions, the boundary layer temporarily thickens corresponding to the regions with the greatest heat transfer where the flow impinges onto the upstream surface of the tows.

Similar behavior is present over the 45° twill shown in Figure 12d, where the plane was taken along the centerline of downstream facing chevrons. As the tows transition from one to another the boundary layer thickens temporarily, similar to but more prominent than over the 0° twill surface.

Over the k-type roughness surface in Figure 12e the boundary layer is similar to the smooth surface except with more prominent low near-wall velocities over the rougher surface. In contrast, the 0° twill + k-type roughness in Figure 12f has a thicker boundary layer similar to the 45° 5HS surface. Near the wall there are some low velocity regions in between tows where separation and recirculation are responsible for local reductions in heat transfer. Further from the wall the local variations are damped out and the boundary layer steadily grows.

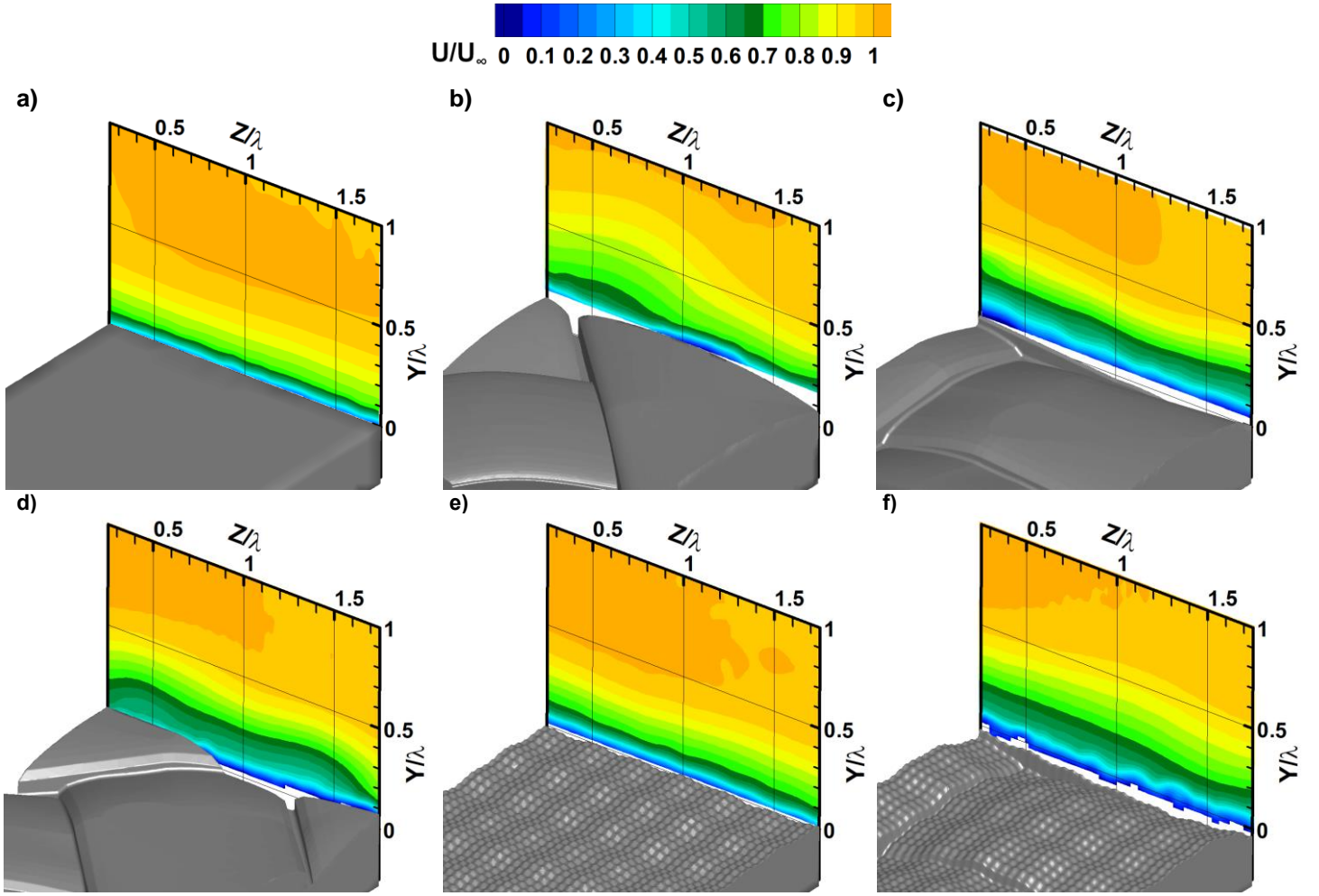


Figure 11. Cross-plane velocity profiles at $x/\lambda=9$, $Re=325000$ and $Tu=0.5\%$ for the a) smooth, b) 45° 5HS, c) 0° Twill, d) 45° Twill, e) k-type, and f) 0° Twill + k-type roughness surfaces

To emphasize the increased vertical motion caused by CMC weaves, Figure 13 shows the wall normal velocity over the 0° twill and 0° twill + k-type roughness with localized regions of flow moving toward (blue contours) and away from (red contours) the wall. Above downward facing regions the flow is moving towards the wall, and above forward-facing protrusions flow is moving away from the wall. This cycle of upward and downward motion creates recirculation bubbles, locally thickening boundary layers across tow transitions.

Figure 14 shows the streamwise velocity fluctuations over the smooth, 0° twill and 0° twill + k-type roughness surfaces (note that stitching of the two separate camera images into the composite long image causes some local discontinuities). The boundary layer over the 0° twill surface in Figure 14b is more active than the smooth surface, with this increased activity increasing fluid transport near the wall leading to heat transfer augmentation. Additionally, although partially obscured by missing data at the leading edge of the tow near $X/\lambda=8$, a localized region of increased turbulence is generated in the same region as the greatest heat transfer values observed in Figure 5d. The thick boundary layer of the 0° twill + k-type roughness

surface in Figure 5g is has even higher turbulence near the wall that is associated with the increased heat transfer over that surface relative to the 0° twill surface.

High Freestream Turbulence Flowfields

High freestream turbulence over the measured surfaces results in significant penetration of high momentum freestream fluid deep into the boundary layer, resulting in higher near-wall velocities as shown in Figure 15 for both the smooth and 0° twill + k-type roughness. Figure 15a shows the developing boundary layer over the smooth surface, where compared to the low turbulence case in Figure 12a, the high turbulence case has higher near wall velocities and smaller observable velocity gradient. The boundary layer over the 0° twill and k-type roughness in Figure 15b manifests as a thicker version of boundary layer over the 0° twill. Over the tested surfaces the increase in near wall velocities is likely the most identifiable indicator of increased heat transfer present in Figures 8 and 9 where the increased velocities help convect heat away from the wall.

The increased velocity present over the rough surfaces at

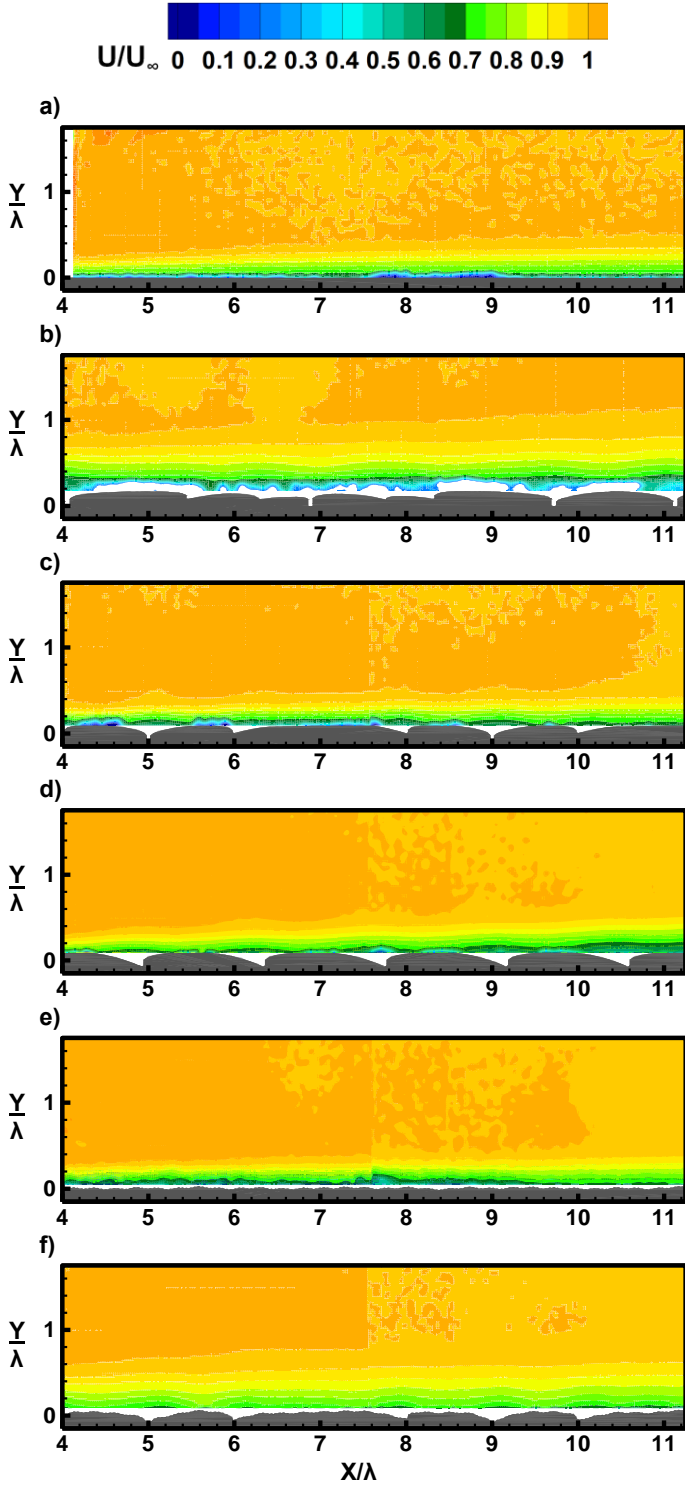


Figure 12. Streamwise velocity profiles at $Tu=0.5\%$ for the a) smooth at $z/\lambda=1.5$, b) 45° 5HS at $z/\lambda=1.3$, c) 0° Twill at $z/\lambda=1.3$, d) 45° Twill at $z/\lambda=1.3$, e) k-type at $z/\lambda=1.5$, and f) 0° Twill + k-type roughness at $z/\lambda=1.3$

elevated freestream turbulence is likely due to the freestream exerting a greater influence into the lower boundary layer. Turbulence intensity over the 0° twill + k-type roughness in Figure 16 is much higher than the low turbulence case in Figure

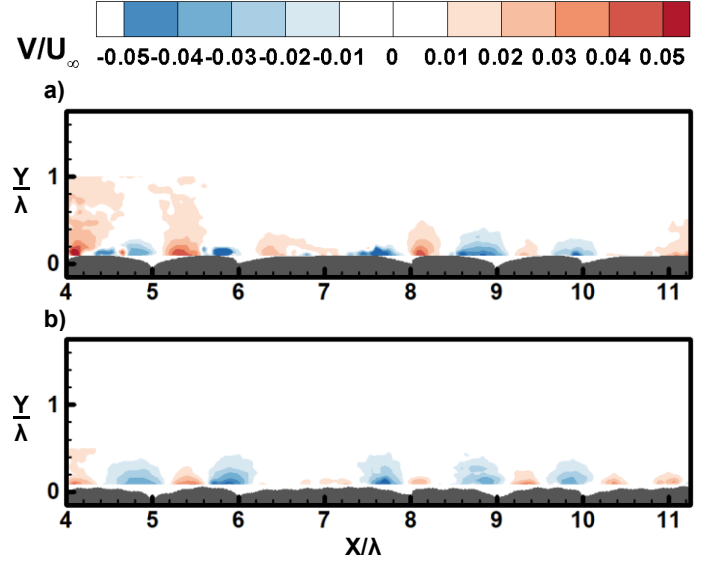


Figure 13. Wall normal velocities over the a) 0° twill at $z/\lambda=1.3$ and b) 0° twill + k-type roughness at $z/\lambda=1.3$

14c. The elevated freestream turbulence dominates the entire flowfield including within the observable boundary layer, increasing the heat transfer at the wall. Downstream of $X/\lambda = 8$ there is an inflection in the streamwise turbulence intensity in a direction normal to the wall, indicating that the turbulence within the developing boundary layer is stabilizing its intensity relative to the decaying level in the freestream. This is why the

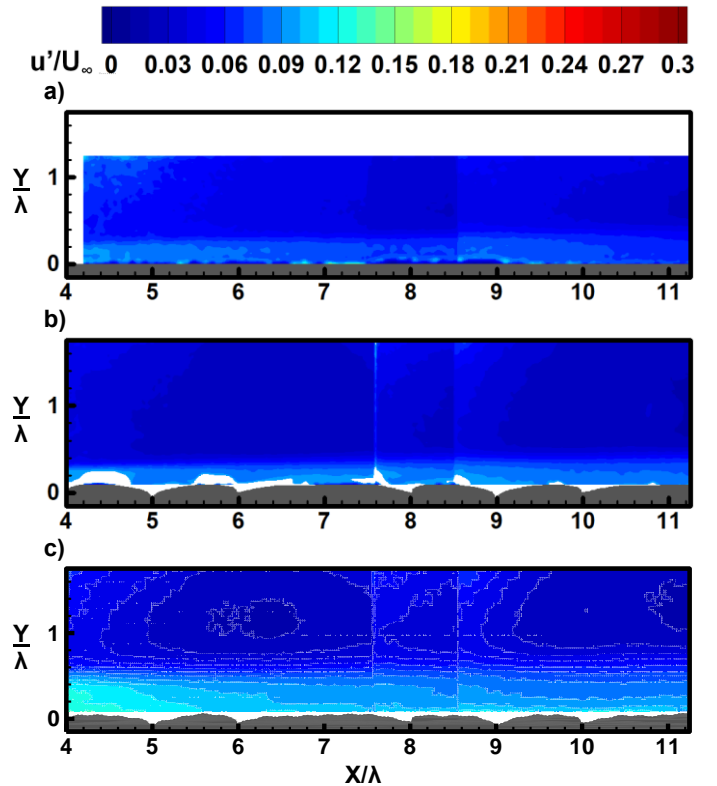


Figure 14. Streamwise turbulence intensity at $Tu=0.5\%$ for the a) smooth at $z/\lambda=1.5$, b) 0° Twill at $z/\lambda=1.3$, and c) 0° Twill + k-type roughness at $z/\lambda=1.3$

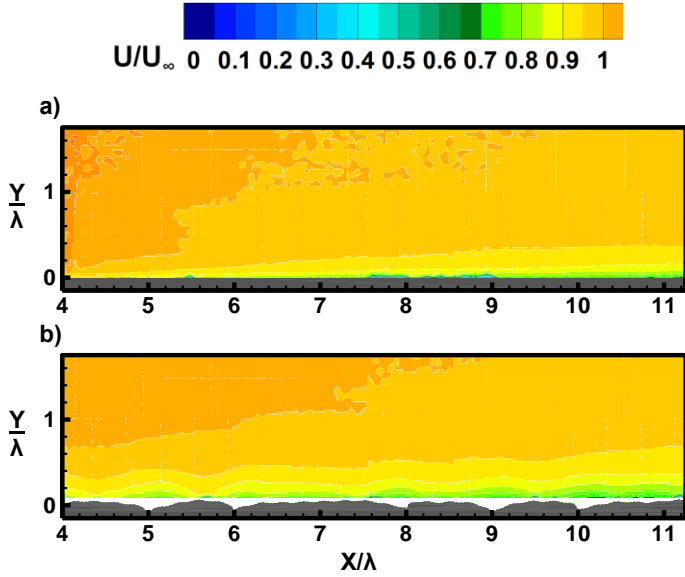


Figure 15. Streamwise velocity profiles at $Tu=24\%$ for the a) smooth at $z/\lambda=1.5$ and b) 0° Twill + k-type roughness at $z/\lambda=1.3$

heat transfer augmentation in Figure 8 eventually becomes similar for both freestream turbulence conditions.

CONCLUSIONS

Individual roughness topographies of CMC surfaces have unique impacts on flowfield and heat transfer performance at both low and high freestream turbulence levels. In general, the amount and exposure of forward-facing surfaces on CMC surfaces results in higher heat transfer over the surface and increased boundary layer thickness, and should be avoided in design if possible.

Weave surfaces oriented at 45° to the freestream appear to have two types of heat transfer behaviors. The 45° 5HS surface with major tow transitions spaced 5λ apart behaves similarly to the 0° 5HS surface with only localized impact to heat transfer, since the asymmetric flow established by the angled tows does not occur frequently enough. Increases in heat transfer from flow impingement are mostly offset by the relative decrease in heat transfer caused by separation on the downstream side of individual tows. The 45° twill surface, however, has a very different behavior. Flow impingement on the repeating upstream facing angled features generates secondary flows similar to the streamwise vortices generated by V-shaped rib turbulators,

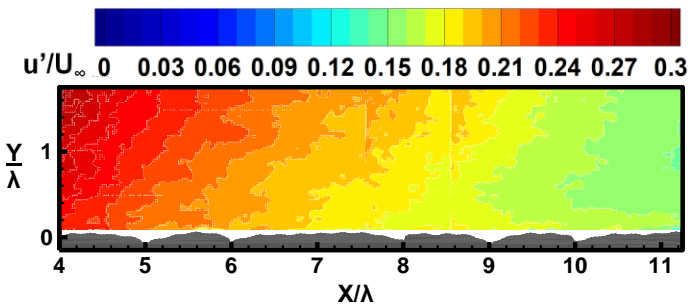


Figure 16. Streamwise turbulence intensity over the 0° twill + k-type roughness surface

which increase heat transfer on upstream-facing chevron shapes by circulating cool upper boundary layer fluid onto those surfaces, while decreasing heat transfer on downstream-facing chevron shapes by circulating warm near-wall fluid onto those surfaces. This also results in large localized disturbances in the boundary layer.

For the scales tested in this work, superimposing small length scale roughness onto larger weave tows creates a surface that has the heat transfer characteristics of both surfaces. Smaller scales from the k-type roughness cause small high frequency variations in local heat transfer across the surface that can be superimposed onto the large lower frequency changes to heat transfer across the weave surface. The additive effect of these two surfaces is likely the result of the large difference in relevant length scales limiting nonlinear interactions; however, this needs to be investigated more fully.

Increasing freestream turbulence over the rough surfaces resulted in similar increases in heat transfer relative to the low-turbulence condition for all of the surfaces tested. This similarity suggests that the turbulence scales of the high freestream turbulence condition do not have a nonlinear interaction with the scales created by the surfaces investigated here, and are simply superimposed on whatever augmentation already exists due to that surface. However, it also means that the additive augmentation effect observed at low freestream turbulence for the 0° twill + k-type roughness surface versus its constituent components does not hold for high freestream turbulence. Future work should identify the mechanisms behind this.

ACKNOWLEDGEMENTS

This material is based upon work supported by the U.S. Department of Energy, Office of Energy Efficiency and Renewable Energy's Advanced Manufacturing Office, under Award Number DE-EE0009407.

REFERENCES

- [1] Levine, S. R., 1992, "Ceramics and Ceramic Matrix Composites - Aerospace Potential and Status," Proceedings of the Structures, Structural Dynamics and Materials Conference, Dallas, Tx USA, AIAA Paper No. AIAA-92-2445-CP, pp. 1942–1947.
- [2] Krenkel, W., 2008, *Ceramic Matrix Composites Fiber Reinforced Ceramics and Their Applications*, Wiley-VCH Verlag GmbH & Co. KGaA.
- [3] Bogard, D. G., Schmidt, D. L., and Tabbita, M., 1998, "Characterization and Laboratory Simulation of Turbine Airfoil Surface Roughness and Associated Heat Transfer," *J. Turbomach.*, 120(2), pp. 337–342. <https://doi.org/10.1115/1.2841411>.
- [4] Gavalda Diaz, O., Garcia Luna, G., Liao, Z., and Axinte, D., 2019, "The New Challenges of Machining Ceramic Matrix Composites (CMCs): Review of Surface Integrity," *Int. J. Mach. Tools Manuf.*, 139, pp. 24–36. <https://doi.org/10.1016/j.ijmachtools.2019.01.003>.

- [5] Kopeliovich, D., 2018, “Advances in Manufacture of Ceramic Matrix Composites by Infiltration Techniques,” *Adv. Ceram. Matrix Compos. Second Ed.*, pp. 93–119.
- [6] Wilkins, P. H., Lynch, S. P., Thole, K. A., Quach, S., and Vincent, T., 2021, “Experimental Heat Transfer and Boundary Layer Measurements on a Ceramic Matrix Composite Surface,” *J. Turbomach.*, 143(6), 061010. <https://doi.org/10.1115/1.4050314>.
- [7] Jiménez, J., 2004, “Turbulent Flows over Rough Walls,” *Annu. Rev. Fluid Mech.*, 36, pp. 173–196. [10.1146/annurev.fluid.36.050802.122103](https://doi.org/10.1146/annurev.fluid.36.050802.122103).
- [8] Flack, K. A., and Schultz, M. P., 2014, “Roughness Effects on Wall-Bounded Turbulent Flows,” *Phys. Fluids*, 26, pp. 101305. <https://doi.org/10.1063/1.4896280>.
- [9] Chung, D., Hutchins, N., Schultz, M. P., and Flack, K. A., 2021, “Predicting the Drag of Rough Surfaces,” *Annu. Rev. Fluid Mech.* 2021, 53, pp. 439–471. <https://doi.org/10.1146/annurev-fluid-062520-115127>.
- [10] Schultz, M. P., and Flack, K. A., 2007, “The Rough-Wall Turbulent Boundary Layer from the Hydraulically Smooth to the Fully Rough Regime,” *J. Fluid Mech.*, 580, pp. 381–405. <https://doi.org/10.1017/S0022112007005502>.
- [11] Flack, K. A., and Schultz, M. P., 2010, “Review of Hydraulic Roughness Scales in the Fully Rough Regime,” *J. Fluids Eng. Trans. ASME*, 132(4), pp. 041203. <https://doi.org/10.1115/1.4001492>.
- [12] Sigal, A., and Danberg, J. E., 1990, “New Correlation of Roughness Density Effect on the Turbulent Boundary Layer,” *AIAA J.*, 28(3), pp. 554–556. <https://doi.org/10.2514/3.10427>.
- [13] Bons, J. P., Taylor, R. P., McClain, S. T., and Rivir, R. B., 2001, “The Many Faces of Turbine Surface Roughness,” *J. Turbomach.*, 123, pp. 739–748. <https://doi.org/10.1115/1.1400115>.
- [14] Bons, J. P., 2002, “St and Cf Augmentation for Real Turbine Roughness with Elevated Freestream Turbulence,” *J. Turbomach.*, 124, pp. 632–644. <https://doi.org/10.1115/1.1505851>.
- [15] McClain, S. T., Hodge, B. K., and Bons, J. P., 2004, “Predicting Skin Friction and Heat Transfer for Turbulent Flow over Real Gas Turbine Surface Roughness Using the Discrete Element Method,” *J. Turbomach.*, 126(2), pp. 259–267. <https://doi.org/10.1115/1.1740779>.
- [16] Dees, J. E., and Bogard, D. G., 2008, “Effects of Regular and Random Roughness on the Heat Transfer and Skin Friction Coefficient on the Suction Side of a Gas Turbine Vane,” *J. Turbomach.*, 130(4). <https://doi.org/10.1115/1.2812338>.
- [17] Wang, Z. J., Chi, X. K., Shih, T., and Bons, J., 2004, “Direct Simulation of Surface Roughness Effects with RANS and DES Approaches on Viscous Adaptive Cartesian Grids,” 34th AIAA Fluid Dynamics Conference and Exhibit, Portland, Oregon, USA, June 28 - July 1, 2004, AIAA Paper No. 2004-2420.
- [18] Bons, J., 2005, “A Critical Assessment of Reynolds Analogy for Turbine Flows,” *J. Heat Transfer*, 127(5), pp. 472–485. <https://doi.org/10.1115/1.1861919>.
- [19] Bons, J. P., 2010, “A Review of Surface Roughness Effects in Gas Turbines,” *J. Turbomach.*, 132(2), pp. 021004. <https://doi.org/10.1115/1.3066315>.
- [20] Mejia-Alvarez, R., and Christensen, K. T., 2010, “Low-Order Representations of Irregular Surface Roughness and Their Impact on a Turbulent Boundary Layer,” *Phys. Fluids*, 22, pp. 015106. <https://doi.org/10.1063/1.3291076>.
- [21] Johnson, B. E., and Christensen, K. T., 2009, “Turbulent Flow over Low-Order Models of Highly Irregular Surface Roughness,” *AIAA J.*, 47(5), pp. 1288–1299. <https://doi.org/10.2514/1.41266>.
- [22] Schultz, M. P., and Flack, K. A., 2009, “Turbulent Boundary Layers on a Systematically Varied Rough Wall,” *Phys. Fluids*, 21, pp. 015104. <https://doi.org/10.1063/1.3059630>.
- [23] Napoli, E., Armenio, V., and De Marchis, M., 2008, “The Effect of the Slope of Irregularly Distributed Roughness Elements on Turbulent Wall-Bounded Flows,” *J. Fluid Mech.*, 613, pp. 385–394. <https://doi.org/10.1017/S0022112008003571>.
- [24] Barros, J. M., Schultz, M. P., and Flack, K. A., 2018, “Measurements of Skin-Friction of Systematically Generated Surface Roughness,” *Int. J. Heat Fluid Flow*, 72, pp. 1–7. <https://doi.org/10.1016/j.ijheatfluidflow.2018.04.015>.
- [25] Nugroho, B., Monty, J. P., Utama, I. K. A. P., Ganapathisubramani, B., and Hutchins, N., 2021, “Non-k-Type Behavior of Roughness When In-Plane Wavelength Approaches the Boundary Layer Thickness,” *J. Fluid Mech.*, 911. <https://doi.org/10.1017/jfm.2020.875>.
- [26] Krishna, K., Ricklick, M. A., 2016, “Preliminary Investigation of an Oblique Jet Impingement Cooling on CMC Rough Surface,” Proceedings of the 52nd AIAA/SAE/ASEE Joint Propulsion Conference, Salt Lake City, UT, USA, July 25–27, 2016, AIAA Paper No. AIAA 2016-4851.
- [27] Krishna, K., and Ricklick, M., 2017, “Heat Transfer Analysis of Jet Impingement Cooling on a Simulated Ceramic Matrix Composite Surface,” Proceedings of the ASME Turbo Expo, Charlotte, NC, USA, June 26–30, 2017, ASME Paper No. GT2017-64991.
- [28] Wilkins, P. H., Lynch, S. P., Thole, K. A., Vincent, T., Quach, S., and Mongillo, D., 2022, “Effect of a Ceramic Matrix Composite Surface on Film Cooling,” *J. Turbomach.*, 144(8), pp. 081010. <https://doi.org/10.1115/1.4053842>.
- [29] Brown, L. P., 2022, “TexGen,” Advanced Weaving Technology, Y. Kyosev, and F. Boussu, eds., Springer, Cham, Cham, Switzerland, pp. 253–291.
- [30] Nemeth, N. N., Mital, S. K., and Lang, J., 2010, Evaluation of Solid Modeling Software for Finite Element Analysis of Woven Ceramic Matrix Composites, NASA T/M 2010-216250.
- [31] Eberly, M. K., and Thole, K. A., 2013, “Time-Resolved Film-Cooling Flows at High and Low Density Ratios,” *J. Turbomach.*, 136(6), pp. 061003. <https://doi.org/10.1115/1.4025574>.

- [32] Schroeder, R. P., and Thole, K. A., 2016, “Effect of High Freestream Turbulence on Flowfields of Shaped Film Cooling Holes,” *J. Turbomach.*, 138(9), pp. 091001. <https://doi.org/10.1115/1.4032736>.
- [33] Wittig, S., Schulz, A., Gritsch, M., and Thole, K. A., 1996, “Transonic Film-Cooling Investigations: Effects of Hole Shapes and Orientations,” Proceedings of the ASME Turbo Expo, Birmingham, UK, June 10-13, 1996, ASME Paper No. 96-GT-222.
- [34] Gritsch, M., Schulz, A., and Wittig, S., 2000, “Film-Cooling Holes with Expanded Exits: Near-Hole Heat Transfer Coefficients,” *Int. J. Heat Fluid Flow*, 21(2), pp. 146–155. [https://doi.org/10.1016/S0142-727X\(99\)00076-4](https://doi.org/10.1016/S0142-727X(99)00076-4).
- [35] Raffel, M., Willert, C. E., Scarano, F., Kahler, C. J., Werely, S. T., and Kompenhans, J., 2018, Particle Image Velocimetry A Practical Guide, Springer International Publishing AG.
- [36] Moffat, R. J., 1982, “Contributions to the Theory of Single-Sample Uncertainty Analysis,” *J. Fluids Eng. Trans. ASME*, 104(2), pp. 250–258. <https://doi.org/10.1115/1.3241818>.
- [37] Figliola, R. S., and Beasley, D. E., 2011, Theory and Design for Mechanical Measurements, John Wiley & Sons, Inc.
- [38] Wieneke, B., 2015, “PIV Uncertainty Quantification from Correlation Statistics,” *Meas. Sci. Technol.*, 26(7). <https://doi.org/10.1088/0957-0233/26/7/074002>.
- [39] Bergman, T. L., Lavine, A. S., Incropera, F. P., Dewitt, D. P., 2011, *Introduction to Heat Transfer*, John Wiley and Sons, NY.
- [40] Flack, K. A., Schultz, M. P., and Barros, J. M., 2019, “Skin Friction Measurements of Systematically-Variied Roughness: Probing the Role of Roughness Amplitude and Skewness,” *Flow, Turbul. Combust.*, 104, pp. 317–329. <https://doi.org/10.1007/s10494-019-00077-1>.
- [41] Taslim, M. E., and Lengkong, A., 1998, “45 Deg Staggered Rib Heat Transfer Coefficient Measurements in a Square Channel,” *J. Turbomach.*, 120(3), pp. 571–580. <https://doi.org/10.1115/1.2841755>.